Journal of the Earth Simulator, Volume 9, March 2008, 3–18

NIES/FRCGC Global Atmospheric Tracer Transport Model: Description, Validation, and Surface Sources and Sinks Inversion

Shamil Maksyutov[1,2], Prabir K. Patra[2]*, Ryo Onishi[1,3], Tazu Saeki[4], and Takakiyo Nakazawa[5,1]

[1] *National Institute for Environmental Studies, Tsukuba, Ibaraki 305-8506, Japan*
[2] *Frontier Research Center for Global Change, Japan Agency for Marine-Earth Science and Technology, Yokohama 236-0001, Japan*
[3] *The Earth Simulator Center, Japan Agency for Marine-Earth Science and Technology, Yokohama 236-0001, Japan*
[4] *Research Institute for Humanity and Nature, Kyoto 603-8047, Japan*
[5] *Graduate School of Science, Tohoku University, Sendai 980-8578, Japan*

(Received June 13, 2007; Revised manuscript accepted January 25, 2008)

Abstract We present description, validation, utilization, and update of the NIES/FRCGC (National Institute for Environmental Studies/Frontier Research Center for Global Change) off-line global atmospheric tracer transport model. The model transport is driven by analyzed meteorological fields and designed to simulate seasonal and diurnal cycles, synoptic variations, and spatial distributions of atmospheric chemical constituents in the troposphere. Tracer transport is simulated with semi-Lagrangian transport algorithm. The vertical mixing by the boundary layer turbulence and penetrative convection are parameterized. We have tested the model performance against observations of radon-222 and SF_6. The long-lived tracer transport properties are also compared to the other models and observations using the simulation of atmospheric-CO_2. Our results suggest that the model can produce realistic interhemispheric exchange rate and vertical tracer distributions in lower and mid troposphere. A new version (NIES05) of the transport model has been developed for simulating diurnally varying CO_2 concentrations at much finer horizontal resolution ($0.25^\circ \times 0.25^\circ \times 47$ level). The high resolution model results show large improvements in match with the observations at a continental site Tsukuba (~50km north-west of Tokyo). The NIES/FRCGC model is adopted to run on Earth Simulator for the purpose of source/sinks inversion of atmospheric-CO_2. We used interannually varying meteorology for the forward simulations of known CO_2 fluxes and normalized emissions from 64 divisions of the globe for which CO_2 fluxes are determined by inverse modeling of atmospheric-CO_2. We have discussed the long-term trends and interannual variability in global and regional CO_2 fluxes. The results suggest weak increases and reduction in total land/ocean and southern ocean sinks, respectively, for the period of 1982-2004. The estimated land flux variabilities have been explained by accounting for ecosystem response to inter-annual climate variability and forest fires.

Keywords: Forward Transport Model, High Resolution CO_2 Simulations, Inverse Modeling of CO_2 Sources/Sinks

1. Introduction

Atmospheric transport has to be accounted for when analyzing the relationships between observations of atmospheric constituents and their sources/sinks near the earth's surface or through the chemical transformation in the atmosphere. The tracer transport modeling is done on different scales from local plume spread, regional mesoscale transport to global scale analysis, depending on scales of the phenomena. The global atmospheric tracer transport models are usually applied to studies of the global cycles of the long-lived atmospheric trace gases such as carbon dioxide (CO_2) and methane (CH_4), because the long-lived tracers exhibit observable global patterns (e.g. interhemispheric gradient of the concentration). Global modeling analysis has helped to identify the relative contribution of the land and oceans in Northern and Southern hemisphere to the interhemispheric concentration differences for CO_2, CH_4, carbon monoxide and other tracer

* ***Corresponding author****: Dr. Prabir K. Patra, Frontier Research Center for Global Change, Japan Agency for Marine-Earth Science and Technology, 3173-25 Showa-machi, Yokohama 236-0001, Japan. E-mail: prabir@jamstec.go.jp*

species (e.g. Bolin and Keeling, 1963; Hein et al, 1997). For the case of the stable and slowly reacting chemical species, a number of studies have derived information on the spatial and temporal distribution of the surface sources and sinks by applying transport model and atmospheric observations (e.g., Tans et al., 1990; Rayner et al., 1999).

In this paper we present the development of a global atmospheric tracer transport model, its application for retrieving CO_2 flux variability by time-dependent inversion (TDI), and finally recent updates for high resolution simulations using improved meteorology. Our main objective is to model the sub-grid scale physical process parameterizations tuned to recent observations, and at the same time trying to maintain flexibility to choose meteorological input, model resolution and other practical considerations. For atmospheric tracers with a lifetime longer than several months, an accurate simulation of interhemispheric transport rate appears to be important for global scale analysis, because it affects critically the results for regional or hemispheric breakdown of unknown fluxes, such as the terrestrial CO_2 sink. Another important feature is a vertical profile of the tracer concentration over emitting regions, influenced by a rate of PBL mixing with free troposphere. Global tracer transport model intercomparison studies (e.g., Jacob et al., 1997; Law et al., 1996; Denning et al., 1999) demonstrated that the sizable difference in vertical mixing rates exists between models, and discrepancies between models and observations appear to be significant for the well established climate and transport models.

2. Model description

In this section, we describe our model design and numerical representation of the model processes, including the model equations, physical processes parameterizations and their numerical realizations. The development of NIES/FRCGC model reported here is to simulate the seasonal cycles of the long-lived tracer species at a relatively coarse grid resolution (2.5 to 5 degrees longitude-latitude), and to perform sources/sinks inversion of atmospheric-CO_2. The transport model has been improved by increasing spatial resolution and driven by diurnal cycle resolving meteorology for simulating diurnal-synoptic scale variations (version: NIES05). Present model version evolved since early 1990s (Akimoto et al., 1993; Maksyutov, 1994; Maksyutov and Inoue, 2000; Maksyutov et al. 2000). Several model algorithms and parameterizations tested in this process and were replaced or refined in order to produce more realistic simulation of the various atmospheric tracers.

2.1 Model equations

We use the terrain following σ vertical coordinate (Philips, 1957), which is defined by expression: $\sigma = p/p_s$, where p and p_S are atmospheric and surface pressures, respectively. Atmospheric constituent transport equation can be presented in the Lagrangian-style form (Williamson and Laprise, 2000):

$$\frac{dq^k}{dt} = \frac{\partial q^k}{\partial t} + \mathbf{V}\cdot\nabla_\sigma q^k + \dot{\sigma}\cdot\frac{\partial q^k}{\partial \sigma} = \frac{\partial}{\partial \sigma}F^k + S^k$$
$$\nabla_\sigma = \frac{\partial}{R\cos(\phi)\partial\lambda} + \frac{\partial}{R\partial\phi} \quad (1)$$

Here q^k is the mixing ratio (volume) in dry air for tracer k, and F^k is the vertical flux of that tracer due to turbulent diffusion and moist convective transport. S^k is the mixing ratio tendency due to surface fluxes and chemical transformations, λ and ϕ are the longitude and latitude in radians, R is the radius of the Earth, and $\mathbf{V}$ the horizontal wind velocity vector with longitudinal and latitudinal components (u, v). $\dot{\sigma}$ is vertical wind velocity in σ-coordinate system ($\dot{\sigma}$=+ve indicates downward motion). Eqn. (1) is solved using single time-level, time splitting scheme, with separate consecutive steps for surface emissions and transformations, semi-Lagrangian transport, vertical mixing by penetrative convection (all explicit), and vertical diffusion by turbulence (implicit). The winds (u, v) are interpolated from the global analysis winds. Vertical subgrid scale fluxes F^k are obtained using parameterizations of the penetrative cumulus convection and PBL climatology. The vertical wind in sigma coordinates $\dot{\sigma}$ is derived diagnostically from the global analysis winds. It is assumed that vertical velocity in global analysis ω represents a mass flow through constant pressure surface, and is prepared using the equation (see Washington and Parkinson, 1986):

$$\omega = p_S\cdot\dot{\sigma} + \sigma\cdot\left(\frac{\partial p_S}{\partial t} + \mathbf{V}\cdot\nabla_\sigma p_S\right), \quad (2)$$

which includes effects of air motion with respect to constant sigma surfaces (as pressure and sigma planes are not parallel) and surface pressure tendency. The $\dot{\sigma}$ is calculated from Eqn. 2 according to

$$p_S\cdot\dot{\sigma} = \omega - \sigma\cdot\left(\frac{\partial p_S}{\partial t} + \mathbf{V}\cdot\nabla_\sigma p_S\right).$$

2.2 Representation of the physical processes: cumulus convection

The vertical redistribution of tracers by cumulus convection is based on cumulus mass-fluxes calculated in a Kuo-type scheme following Grell (1995), and modified to include entrainment and detrainment processes on convective updrafts and downdrafts proposed by Tiedtke (1989). In this formulation the cloud base level σ_c is

obtained by adding small perturbation to humidity and temperature at levels below 700 hPa and adiabatically lifting the air parcel until the condensation occurs. For cloud base σ_c we use the lowest level where condensation would occur, known as lifting condensation level. The supply rate of moisture available for penetrative convection is then estimated. The horizontal moisture divergence is evaluated from analysis winds and water vapor content (threshold at the cloud base is set to 0.0002 kg/kg). Low-level moisture convergence M_1 is obtained by integrating the horizontal moisture convergence below cloud base level:

$$M_1 = -\left[\int_{\sigma_c}^{1} \nabla_\sigma (p_S \cdot \mathrm{V} \cdot q)\, d\sigma - M_c\right] + S_{evap}. \qquad (3)$$

S_{evap} is the surface evaporation. For evaporation climatology, we use monthly surface evaporation fields by NASA GEOS-1 reanalysis for 1992-1993 (Schubert et al., 1993). Use of the monthly evaporation rate for estimating the moisture divergence has been tested by Heimann (1995). To account for deviation from the mass conservation in the wind data the moisture divergence term is corrected for non-zero divergence of the air mass M_c:

$$M_c = \int_{\sigma_c}^{1} q \cdot \nabla_\sigma (p_S \cdot \mathrm{V})\, d\sigma.$$

The mass flux M_u in updraft is set to M_1 divided by water vapor mixing ratio at cloud base q_{base}, so that $M_1 = M_u \cdot q_{base}$. The vertical profiles of entrainment and detrainment rates are set proportional to M_u in accordance with Tiedtke (1989). The cloud top is determined by comparing the virtual potential temperatures in the updraft and environment, for which an overshot of 3 degrees K is allowed. The clouds thinner than $\Delta\sigma = 0.1$ are excluded. The downdraft mass flux is set to 0.2 of that in the updraft. The vertical distribution of zonal average cumulus mass flux on updrafts is presented on Fig. 1, which clearly shows the location of the tropical convective cell moving along with the seasonal changes in solar insolation, from southern hemisphere in January to northern hemisphere in July. Also the overall seasonal features in mid-latitude convective zones are well captured.

The tracers are transported vertically by applying a simplified explicit scheme. It is assumed that the updrafts and downdrafts make only a negligibly small part of a grid column; the rest is designated as environment air. First the vertical profiles of the concentrations in the updraft and downdraft air are computed taking into account rates of mixing with environment air by entrainment and detrainment, than the concentration tendencies in environment air are obtained from entrainment/detrainment rates.

2.3 Representation of the physical processes: turbulent diffusion

We used climatological planetary boundary layer (PBL) height to separate transport processes in the well-mixed PBL and free troposphere. The monthly averages of daily maximum PBL thickness data are prepared from 3-hourly PBL height data at GEOS-1 reanalysis dataset for 1992–1993 (Schubert et al., 1993). Daily maximum height is selected to representative time of trace gas observations. The summer-time PBL height over mid-lat-

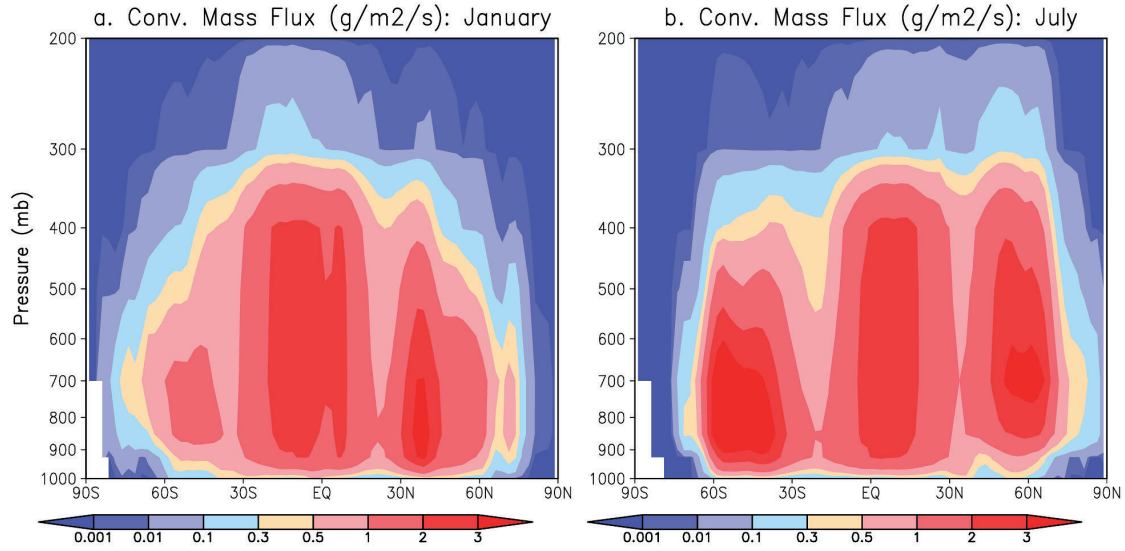

Fig. 1 An example of zonal average convective mass fluxes for January and July as estimated by the model.

itude continental areas varies around 150 hPa, approximately 1.5 km. The optimal procedure to derive the monthly PBL climatology can be debated. The other problem is lack of day to day variability. To overcome this problem and more realistic simulation of diurnal cycle, newer version of the model (version: NIES05) uses diurnally varying PBL heights at 3 hourly interval from ECMWF analyzed and forecasts products.

Below PBL top, the turbulent diffusivity is set to a constant value of 40 $m^2\ s^{-1}$. The large scale transport such as zonally-averaged vertical profiles of constituents does not change appreciably by decreasing the diffusivity to 20 $m^2\ s^{-1}$. The selection of the turbulent diffusivity value inside the PBL seems to be not critical as far as vertical profiles in well-mixed daytime conditions are concerned (in the older version). Above the PBL top the turbulent diffusivity K_T is calculated using local stability function, as in Hack et al. (1993):

$$K_T = l^2 \cdot S \cdot F_S(Ri).$$

Here l is the mixing length, l = 30 m. $S = \left|\frac{\partial V}{\partial z}\right|$ is the vertical wind shear, Ri is local Richardson number, defined by temperature and wind gradients as:

$$Ri = \frac{g}{S^2} \cdot \frac{\partial \ln \theta_V}{\partial z}.$$

θ_V is the virtual potential temperature, g is the acceleration of gravity. Stability dependent function $F_S(Ri)$ is defined as:

$$F_S(Ri) = (1 - 18 \cdot Ri)^{\frac{1}{2}} \quad \text{for unstable conditions } (Ri < 0)$$

and

$$F_S(Ri) = 1 - \frac{Ri}{Ri_C} \quad \text{for stable conditions } (0 < Ri < Ri_C),$$

where $Ri_c = 0.2$ is a critical Richardson number, above which $F_S(Ri) = 0$.

2.4 Semi-Lagrangian transport and trajectory calculation

Semi-Lagrangian transport algorithm is an effective way to solve the tracer transport problems in a polar coordinate system (Williamson and Rasch, 1989), as opposed to the regular-grid schemes formulated in flux form, that have a singularity near the poles caused by small grid size in longitudinal direction. In the semi-Lagrangian approach the tracer concentration change due to transport from initial state (time t_0) to new value at next time step $t_0 + \Delta t$ is evaluated in 2 steps:

Step 1 (Trajectory calculation): For the each grid point location a three-dimensional trajectory is calculated for an air parcel, which arrives to that grid point at time $t_0 + \Delta t$. The trajectory location at time t_0 is designated as departure point, and the trajectory itself is called a back trajectory, because it is calculated backward in time.

Step 2 (Interpolation): A concentration at departure point at time t_0 is obtained using interpolation from nearby grid point values. In the absence of mixing and transformation processes, concentration at arrival point should be exactly same as that at the departure point, thus the tracer concentrations at new time step $t_0 + \Delta t$ are set to those at corresponding departure points.

The trajectories are calculated using explicit integration of the air parcel motion in the Cartesian coordinate system originated in the Earth center. The coordinate transformation from polar to Cartesian coordinate system and back is used on the each time step. Calculation of the departure point on each time step is done in 3 sub-steps:

a) Interpolate wind and pressure to the current air parcel position in polar coordinates, using bilinear approximations.
b) Convert the winds and air parcel coordinates to Cartesian coordinate system centered at the Earth center, and calculate displacement tangent to Earth surface.
c) Convert new position back to polar coordinate system and finding sigma level change by integrating vertical motion.

We provide here a short description of the trajectory calculation equations (as referred in Step 1 above). The horizontal (parallel to Earth surface) air parcel movement is determined in the earth-centered coordinate system. The earth centered system has x–axis passing the point on the Earth surface at 0°E, 0°N; y-axis passes via 90°E, 0°N, z-axis passing via 90°N. Horizontal motion in polar coordinates (λ, ϕ) can be represented as

$$R \cdot \cos(\phi) \frac{d\lambda}{dt} = u, \quad R \cdot \frac{d\phi}{dt} = v.$$

The air parcel displacement in the earth-centered system is given by

$$dx = -\delta\phi \cdot \sin(\phi) \cdot \cos(\lambda) - \sin(\phi) \cdot \delta\lambda$$
$$dy = -\delta\phi \cdot \sin(\phi) \cdot \cos(\lambda) - \sin(\phi) \cdot \delta\lambda,$$
$$dz = -\delta\phi \cdot \cos(\phi)$$

where dx, dy, dz are the air parcel displacements in x, y, z directions in the earth-centered coordinate system. $\delta\lambda$, $\delta\phi$ are displacements in longitude, latitude directions and calculated as:

$$\delta\lambda = u \cdot \Delta t = u/(R\cos\phi)\,\delta t,\ \delta\phi = v \cdot \Delta t = (v/R)\,\delta t.$$

Here Δt is the time step (negative for back-trajectory). A new position of the air parcel is given by

$$x = R \cdot \cos(\phi) \cdot \cos(\lambda) + dx$$
$$y = R \cdot \cos(\phi) \cdot \sin(\lambda) + dy.$$
$$z = R \cdot \sin(\phi) + dz$$

x, y, z are longitude, latitude height position of the air parcel, R is radius of the Earth. After the position in the earth-centered coordinate system is determined, the position in the polar coordinate system is given by: $\phi = \arctan\left(z/\sqrt{x^2 + y^2}\right)$ $\lambda = \arctan(y/x)$.

This trajectory calculation module has been extensively used for analysis of the relationship between the atmospheric transport and observed time series of the long-lived tracers such as nitrous oxide (Tohjima et al., 2000), methane (Tohjima et al, 2002) and ozone (Pochanart et al., 2001). The studies where performed with the same wind and trajectory calculation algorithm as in present 3-D transport model, and a good correlation was observed between the variations of the atmospheric composition and trajectory pathways over a time periods extending from 1994 to 1999. Those results give us some degree of confidence in the model's horizontal transport performance.

2.5 Model grid

The model's horizontal and vertical resolutions match those of the meteorological dataset when possible. We use pressure level ECMWF operational analyses at 12-hour time step and 2.5 degrees horizontal resolution in model validation experiments, and NCEP reanalysis data at same resolution for multiyear inverse model simulations (ECMWF, 1999; Courtier et al., 1998). Same horizontal resolution is used in the model; however, the grid layout is different from the meteorological dataset. The first model grid cell on a horizontal plane is located near South Pole, and is confined between (0˚E, 90˚S) and (2.5˚E, 87.5˚S), the last one, at North Pole, is confined between (357.5˚E, 87.5˚N) and (0˚E, 90˚N). Vertical grid layout was designed to provide enough layers to match the resolution of the wind dataset (ECMWF operational analyses), and the variability in the boundary layer height. The validation tests were performed with 15 layer vertical grids, which have slab centers at σ_K = {.97, .93, .89, .85, .775, .7, .6, .5, .4, .3, .25, .2, .15, .1, 0.03}. The slab interfaces are at mid levels $\sigma_{K+1/2} = (\sigma_K + \sigma_{K+1})/2$. Model grid is staggered in vertical dimension. Turbulent diffusivities, convective mass fluxes are assigned to slab interfaces $\sigma_{K+1/2}$, while the winds, temperature, humidity, constituents are assigned to slab centers σ_K. The winds are interpolated from the meteorological analysis grid to the model grid using bilinear interpolation in longitude and latitude in log-pressure coordinate.

The NIES05 model version uses meteorological data by NCEP operational analyses at 26 levels and 1×1 degree resolution at 6 hourly interval and the model simulations are performed at varied horizontal resolution; e.g., 0.5×0.5, 1×1, and 2×2 degrees. This version has 47 vertical layers.

2.6 Mass fixer description

The total tracer mass tendency by the semi-Lagrangian transport algorithm usually deviates from zero, which is often negligible in short term but can disturb the global trends and tracer budgets in long-term simulations. A variety of mass fixers are applied in transport models in order to keep total tracer mass unchanged during transport (Hack et al., 1993; Rasch et al., 1995). We distribute the required correction proportionally to local advection tendencies as described in Taguchi (1996). The mass fixer is designed to conserve as total tracer mass, which is calculated as an integral (with constant factor omitted):

$$M_q = \int_0^1 \int_{-1}^1 \int_0^{2\pi} p_S \cdot (1 - 0.61 \cdot q_W) \cdot q \cdot d\lambda \cdot d(\sin\phi) \cdot d\sigma \quad (4)$$

Here q_w is the water vapour mixing ratio, so $(1–0.61 \cdot q_w)$ is the dry air mass fraction. Mass fixer is designed to conserve M_q by balancing the positive and negative tendencies. The constraint for tracer tendencies on each time step is derived from mass balance equation Eqn. 4 as follows

$$\frac{\partial}{\partial t} M_q = \int_0^1 \int_{-1}^1 \int_0^{2\pi} \left\{ p_S \cdot \left(1 - 0.61 \cdot q_W\right) \cdot \tilde{\dot{q}} + q \cdot \frac{\partial}{\partial t}\left[p_S \cdot \left(1 - 0.61 \cdot q_W\right)\right] \right\} \cdot d\lambda \cdot d(\sin\phi) \cdot d\sigma = 0.$$

Here $\tilde{\dot{q}}$ is the corrected tendency for each tracer. We apply two different factors a_p, a_n as multipliers for positive and negative tendencies so that

$$\tilde{\dot{q}} = \dot{q} \cdot \left[a_p \cdot \theta(\dot{q}) - a_n \cdot \theta(-\dot{q})\right],$$

where $\dot{q}$ is tracer tendency from semi-Lagrangian transport step, $\theta(\dot{q})$ is the step function ($\theta(x) = 1$ for $x \geq 0$, and $\theta(x) = 0$ for $x < 0$). The condition $\max(a_p, a_n)$ is enforced to keep the solution monotonic.

Recent tests conducted for TransCom 3 intercomparison experiment (Gurney et al., 2002) revealed that the mass fixer we use does have a detectable non-local ("teleconnection") effect. It is caused by values of a_p and a_n being slightly different for each particular tracer. The values of a_p and a_n influence the rate of interhemispheric

transport, and the difference is generally larger than that for other mass fixers (R. Law, personal communication, 2001), such as flat concentration adjustment (Hack et al., 1993).

2.7 Treatment of the surface emission-sink fields and chemical transformations

The model is designed to handle constant surface emission fields and seasonally changing emissions in the form of 12 monthly average fields per year. The NIES05 version can ingest fluxes at higher frequency, at up to hourly time interval. The monthly average emissions are interpolated linearly to daily values, on the 15th of each month the emission rate is equal to the monthly average for that month as provided by emission inventory files. The emission inventory fields have higher resolution (e.g., 1×1 degree), than the model grid (e.g., 2.5×2.5 degrees), so the input dataset is mapped to a model grid by counting the overlap area of each input data cell to all model grid data cells. That assures that the global total emission flux is conserved during interpolation.

3. Validation of NIES/FRCGC global transport model

An effective way to validate the atmospheric transport models is by simulating the non-reacting or slowly reacting atmospheric tracer species with well-known emissions and transformations. The tracers of choice are both short lived like radon-222 for diagnosing local/regional transport (Jacob et al., 1997), and long-lived species for evaluating large scale/interhemispheric transport such as SF_6 (Denning et al., 1996; Levin and Hesshaimer, 1996; Maiss et al., 1996), ^{85}Kr (Jacob et al., 1987; Heimann and Keeling, 1989; Zimmermann et al., 1989), chlorofluorocarbons (Prather et al., 1987; Mahowald et al., 1997). General requirements to the suitable tracer species can be summarized as follows: a) availability of reliable emission inventory; b) stable emissions with little seasonal and diurnal variations; c) availability of the observations at required temporal and spatial scales. Most of naturally emitted gaseous species like carbon dioxide, methane, and carbon monoxide can not be used for the model validation because of the large and poorly known spatial-temporal variability of their sources and sinks. Among the most widely used are the gases of the anthropogenic origin – SF_6 and chlorofluorocarbons, because their emission rates are constrained by both the industrial statistics and the trends in global atmospheric content and in addition have no known chemical loss in the troposphere. On the other hand radon-222 (atmospheric residence time of 3.8 days) is emitted only naturally, but its emission rate is related to stable factors, such as type of soil and rocks, rather than the changing vegetation or weather conditions.

We evaluate the model's overall performance using results from several extensively tested global tracer transport models and comparing our model simulations with observations. Those model simulations include the WCRP model intercomparison experiment for radon (Jacob et al., 1997), TransCom experiment (Law et al., 1996) for CO_2 transport intercomparison, and SF_6 transport intercomparison experiment TransCom 2 (Denning et al., 1996). These modeling setups were developed by large transport modeling community, and provide concise and tested set of atmospheric observations and surface emission fields. This gives us an opportunity to concentrate on limited number of key and integral simulated tracer field parameters. The limited set of tests may not actually substitute running the comprehensive validation using large variety of observations (e.g., Dentener et al., 1999), but can still give valuable information on the model performance in terms of large scale averages.

3.1 Evaluation of vertical transport using simulation of radon

Radon-222 is a product of radium-226 decay and has a lifetime of 3.8 days in the atmosphere. The surface radon emission rate varies considerably from 0.5 to 2 atoms cm^{-2} s^{-1}; the emission is suppressed by poorly conducting wet soils and snow cover. Yet there is no better choice of relatively short-lived and widely observed tracer for validating a transport model for continental and remote oceanic atmosphere, and between boundary layer and free troposphere. For validating the model performance using transport of radon-222, we follow the World Climate Research Program (WCRP) inter-comparison experiment specification (Jacob et al., 1997). Radon-222 surface fluxes were set to 0.005 atoms cm^{-2} s^{-1} for oceans and 1 atom cm^{-2} s^{-1} over land between 60°S to 60°N, and to 0.005 atoms cm^{-2} s^{-1} for land between 60°N to 70°N.

The observed and simulated radon concentrations for different heights at Crozet, Hawaii and Cincinnati are compared (not shown) by using the data at Cincinnati (Gold et al., 1964), Crozet (Lambert et al., 1995), and Hawaii (Kritz et al., 1990). The model appears to underpredict surface concentrations at Cincinnati and upper atmospheric observations over Hawaii (200 hPa level), and slightly over-predict the observations at Crozet island. Worth mentioning, however, that several models that participated in Jacob et al. (1997) inter-comparison also failed to capture observed variability in the upper troposphere and reproduce the high radon observed values at 200 hPa over Hawaii. Crozet Island is located south of African coast; the data indicate low background concentrations of below 10^{-21} mol mol^{-1}, with infrequent

high radon episodes lasting few days. In case of Crozet, Jacob at al. (1997) found that the low background concentrations are over-predicted; but the amplitude of the high radon episodes is captured more successfully by the "established" transport models, which is believed to be an indication of models' ability to transport radon to remote atmosphere without significant amplitude loss due to diffusion. The summer maximum at Crozet in our model is within the range of the observed variability.

Figure 2 shows the comparison for winter and summer averages together with other model results as presented by Jacob et al. (1997). The comparison to the observations concludes that our model performs similar to the established three-dimensional transport models (see Fig. 2 caption for details), and the model simulated vertical profiles are close to observed ones. The model results are within the range of observations (widened by observed variability) for all but summer mixed layer value. Even in later case it is close to lower bound of the observation ranges. This may indicate that the summertime mixing (ventilation of the boundary layer) is stronger than that occur in the real world. Same conclusion is also applicable to some other transport models as well (see Fig. 2). However this low value is not conclusive evidence in the view of the fact that the local emission rate uncertainty could be as high as 50%.

3.2 Evaluation of interhemispheric transport using long-lived gases

The validation of the inter-hemispheric and vertical transport became more reliable with the increasing availability of the observational data on a stable tracer, SF_6,

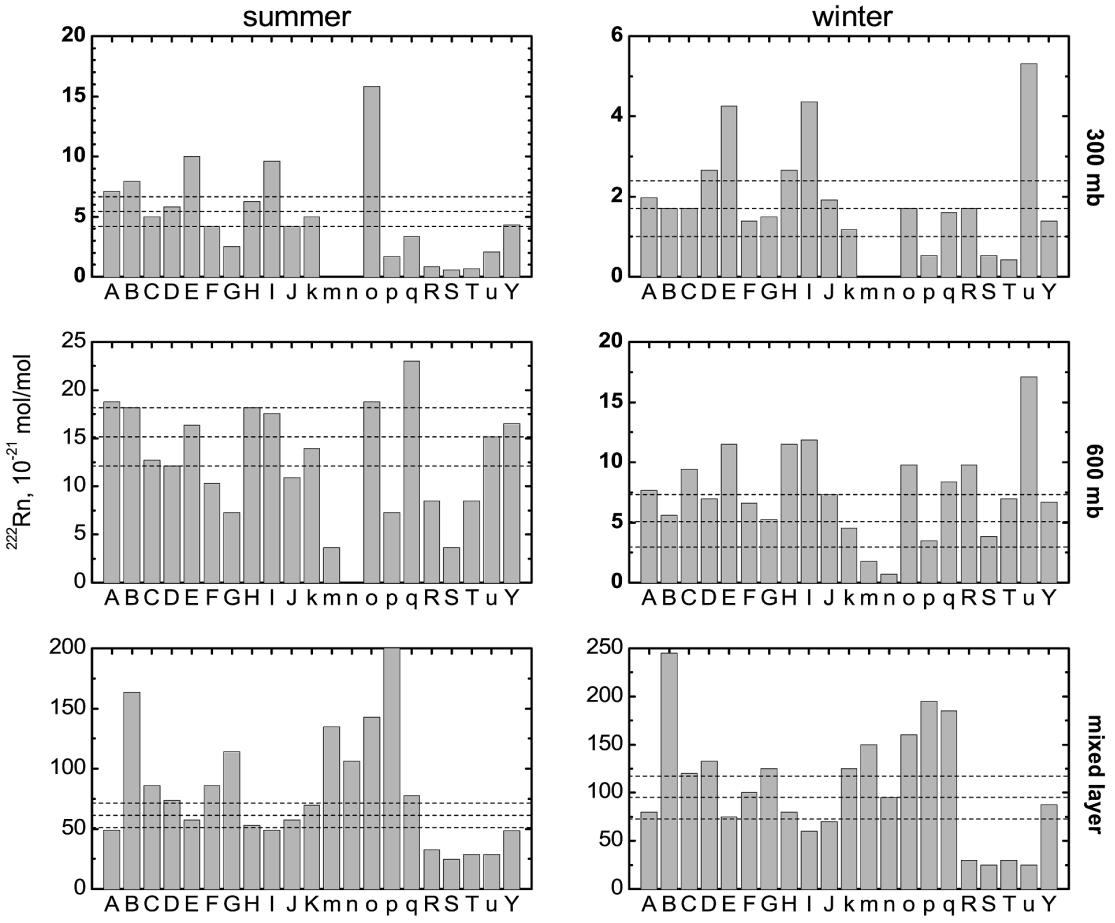

Fig. 2 Comparisons between observations and model simulations of radon-222 averaged for 3 continental sites during winter and summer. Results at three vertical levels (surface, 600 mb and 300 mb) are shown. Models A to J are established three-dimensional models, models k to q are three-dimensional models under development, R to U are two-dimensional models, and Y is for this model. Observations are taken at Cincinnati (40°N, 84°W), Socorro (34°N, 107°W) and Kirov (58°N, 49°E). Different model results are designated by letters along the x-axis: A. CCM2, B. ECHAM3, C. GFDL/ZODIAC, D. GISS/H/I, E. KNMI/TM2, F. LLNL/GRANTOUR, G. LLNL/E, H. LMD, I. TM2Z, J. MOGUNTIA, k. CCC-GCM, m. LaRC, n. LLNL/IMPACT, o. MRI, p. TOMCAT, q. UGAMP, R. AER, S. UCAMB, T. HARWELL, u. UW, Y. NIES/FRCGC (this work).

which can be analyzed accurately in the laboratory after sampling to flasks, has a long atmospheric lifetime of more than 3000 years (Ravishankara et al., 1993), has steady emissions, verifiable via global atmospheric abundance observations (Levin and Hesshaimer, 1996; Geller et al., 1997). We follow the TransCom 2 protocol (Denning et al., 1999) in applying the global emission scenario for SF_6, and present the 5-year simulation that starts from globally homogeneous concentration of 2 pptv (parts per trillion volume) at the beginning of 1989. In Denning et al. (1999) intercomparison the initial value was set to 2.06 pptv, and that resulted some overestimation of the global 1993 average by all models. They had to scale down the concentration increase by a factor of 0.936, which may be interpreted as same amount of decrease in emission rate considering linearity in SF_6 transport.

The annual average of simulated SF_6 concentration for 1993 is compared to the observations compiled by Denning et al. (1999) and plotted in Fig. 3. The common problems that can be observed with both our model and models reported by Denning et al. (1999), are large mismatch for Barbados (13°N, 59°W), and large variability in mismatch for continental and background Northern hemispheric background locations. The pole-to-pole difference (South Pole to Alert) is captured fairly well by our model. Similar simulations of fossil fuel component of CO_2 flux are also conducted. We estimate an interhemispheric exchange time of about 1.5 year and 0.9 year by considering the hemispheric means of surface concentrations and values integrated for the whole hemisphere, respectively.

According to the data presented, the model in a given configuration tends to under-predict inter-hemispheric gradient in background locations by 10% of interhemispheric difference (taken as 0.4 pptv), but at the continental sites the difference can be both positive and negative. The average mismatch is comparable to that by other established transport models in TransCom 2 intercomparison, but indicates that there are scopes for further improvements in forward modeling as well as the spatial distribution of SF_6 emission. The wish list for those improvements would include: a) increasing the interhemispheric gradient in background atmosphere by extra 10% to improve the match between model and observations at background locations, and b) at the same time keep the match at continental locations within present level. The later action would require enhancing the vertical mixing in lower troposphere potentially leading to widening the mismatch with radon-222 data as in Fig. 2. Some these improvements are introduced in the NIES05 version of the model and some results have been discussed later.

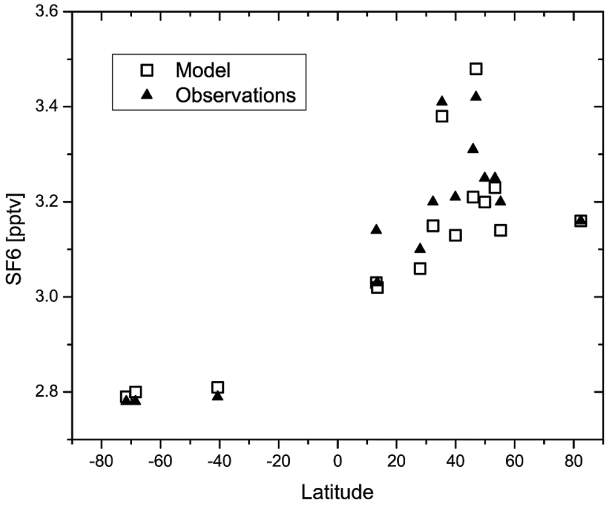

Fig. 3 Interhemispheric gradients in modeled and observed SF_6 concentrations during 1993 are depicted. The modeling set up for this simulation is similar to TransCom 2 experiment (see text).

3.3 CO_2 transport simulation with TransCom 1 experimental protocol

Another test of the model performance is given by the TransCom 1 intercomparison study, which provides the handy set of parameters for evaluating the both horizontal (interhemispheric) and vertical tracer transport by comparison with the established models. Here we report the simulation results for "fossil fuel CO_2" tracer, as specified by Law et al. (1996). The fossil fuel CO_2 source field derived by Inez Fung is same as in Tans et al. (1990), and is based on CO_2 emission inventory by Marland (1989). The results are presented as averages for North and South Hemispheres for surface level, 500 hPa, and 200 hPa levels. The interhemispheric concentration gradient defined as difference in hemispheric averages simulated by our model and models reported by Law et al. (1996) are summarized in Fig. 4. According to previous studies with short/long-lived tracers, such as Jacob et al. (1987), Denning et al. (1999), the extensively validated models such as GISS and TM2 are capable of reproducing the interhemispheric gradient of the long-lived tracers with the accuracy of about 10% or better. We use the same yard-stick for evaluating the performance of our model. NIES/FRCGC model is not considerably different from TM2 in terms of the North-South difference at surface. Along with several other global tracer transport models it predicts about 3-ppm difference at surface, however there is a difference in vertical profile of interhemispheric gradient. At the level of 500 hPa, the relative difference between models becomes larger with TM2 and GISS showing larger interhemispheric difference as compared to others. At 500 hPa our model also produces larger gradient than other models, and difference from TM2 is

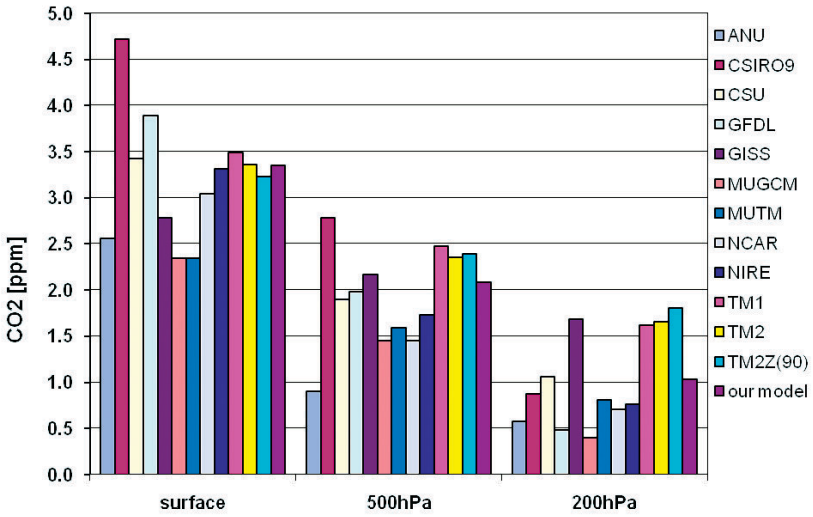

Fig. 4 Interhemispheric gradients in fossil fuel CO_2 tracer simulated by TransCom 1 models and NIES/FRCGC model are shown for three vertical levels.

minor. That is not the case at 200 hPa level. As one can see on Fig. 4, the North-South difference at 200 hPa is as large as 1.5 ppm for GISS and TM2, and about 1 ppm or less for our and other models. Main reason is a stronger vertical transport in GISS and TM2 models, which also makes smaller the model simulated difference between continental boundary layer and background oceanic air, as discussed in Law et al. (1996) and Denning et al. (1999).

4. Introduction to High resolution model version (NIES05)

While the NIES/FRCGC model successfully captures overall features in tracer transport and being used for CO_2 sources/sinks estimation by inverse modeling of atmospheric-CO_2 (section 5), there are increasing demands for simulating tracer distributions at sub-daily time and local scales. Presently about 30 stations are observing atmospheric CO_2 using in situ deployed instruments and provide hourly average values for scientific research (WDCGG, 2007). To understand the observed variability, the transport model simulations are required to be performed at increased spatial resolution and driven by diurnally varying meteorology. We have run our transport model (version NIES05) as high horizontal resolution as 0.25×0.25 degree longitude-latitude, in order to investigate the impact of grid resolution on global CO_2 transportation. Here, we present our simulation results at 4 horizontal resolutions; 2×2, 1×1, 0.5×0.5 and 0.25×0.25 degrees. The vertical resolution is enhanced to 47 levels for better resolving the mixing processes in the boundary layer. For resolving the diurnal variations in surface concentrations, the NIES05 model version is driven by 3-hourly PBL height data from ECMWF analyzed and forecast products (http://www.ecmwf.int; path:/products/data/operational_system). The other 2-D and 3-D meteorological parameters, e.g., sea-level pressure, winds, temperature, are taken from NCEP final analysis (http://dss.ucar.edu;path:/datasets/ds083.2/). Computational demand increased many-fold to run the model at 0.5×0.5 degree horizontal resolution and 47 vertical level; e.g., time and memory size required for one month simulation of 3 tracers are 1.4 hours in real time and 4.4 GB, respectively on 6 CPUs of Earth Simulator (NEC SX-6 series processor).

Three surface CO_2 fluxes are used; SiB3 hourly varying terrestrial ecosystem flux (Denning et al., 1996), seasonally varying ocean flux (Takahashi et al., 2002) and anthropogenic fossil fuel emissions (Marland, 1989) following the TransCom continuous experiment protocol (Law et al., 2006). Higher resolution anthropogenic CO_2 emission distributions are generated from 1×1 degree emission inventory, by redistributing the fluxes spatially following the 2.5min global population map data (CIESIN, 2000), and combined with lower resolution ecosystem and oceanic flux data. This redistribution procedure for fossil fuel emission is an approximation and should ideally be placed according to the source locations. The summation of those fluxes is considered as the total CO_2 surface flux. August 2002 is selected as the target period of our test simulation. The preceding simulation (spin-up run) is performed at 2×2 degree horizontal resolution for the period of 1st January to 31st July, 2002 in order to obtain realistic spatial CO_2 gradients. Figure 5 shows the snapshots of surface CO_2 distributions over East Asia at the resolutions of (a) 2×2 and (b) 0.25×0.25 degree. Though the area-averages concentrations are sim-

ilar in both cases, the distribution patterns are quite different from each other. For example, Figure 5b shows much clearer city plumes than Fig. 5a. It also shows clearer vortex shape due to a typhoon near the Kyusyu area (130˚E, 30˚N).

Figure 6 shows a comparison of atmospheric CO_2 data at Tsukuba 200m tall tower with NIES05 model results at different horizontal resolutions. Tsukuba is located close to a large anthropogenic CO_2 emission region around Tokyo (distance ~ 50 km). The observation data are provided by Y. Sawa and H. Matsueda of Meteorological Research Institute (MRI), Tsukuba (also available at WDCGG website). Each simulation result has its offset value, which is determined from the average value in the August. The higher-resolution simulations have stronger diurnal changes, which are more consistent with observed diurnal cycle. Furthermore, they produce better predictions, particularly during the 3rd to 7th August period when winds from Tokyo dominate. Model simulations at horizontal resolution of 1×1 degree or coarser do not resolve the separation between Tokyo and Tsukuba emissions and transport as Tokyo and Tsukuba reside within the same grid cell and sampling grid do not accurately represents Tsukuba (see Fig. 6 caption). The nearest north-eastern model grid is selected for sampling, and the distance between model grids and Tsukuba are estimated to be about 128, 58, 23 and 8 km for 2×2˚, 1×1˚, 0.5×0.5˚ and 0.25×0.25˚ horizontal resolutions, respectively. Thus the highest resolution run enables us to capture the CO_2 variabilities more realistically compared to the coarse resolution runs.

The simulations of CO_2, radon-222 and SF_6 at hourly, daily and synoptic time scales are being evaluated under the TransCom continuous intercomparison project (Law et al., 2006). Though the first forward simulation results are encouraging this model version will not be used in surface CO_2 sources/sinks inversion for resolving flux variabilities at high spatial and temporal resolutions, until a rigorous evaluation of model simulations of the above mentioned species is completed.

5. Inverse modeling of CO_2 sources and sinks

Using the NIES/FRCGC model version (2.5×2.5 degrees horizontal resolution and 17 vertical layers) we have employed a 64-region time-dependent inverse model (TDIM) for deriving CO_2 fluxes at monthly time interval from atmospheric-CO_2 data at 87 stations. Our 64-region TDIM is based on that has been used in Rayner et al. (1999) and partially follows the TransCom3 protocol (Gurney et al., 2000). The results have been widely reported by analyzing interannual variability in fluxes (Patra et al., 2005a,b), and for understanding the anomalous CO_2 growth rate at Mauna Loa during 2001–2003 (Patra et al., 2005c). Fluxes for oceanic regions have been validated in comparison with independent oceanic-pCO_2 inversion and explored for mechanistic understanding of the flux variabilities using biogeochemical models of land and ocean (Patra et al., 2006b, 2007). Here we will present some recent developments that support the derived flux variabilities and trends by our TDIM setup. In addition, NIES/FRCGC model has been utilized exclusively for optimization of futuristic surface observation networks and to study utility of satellite measurements in surface sources/sinks estimation. Most of these studies

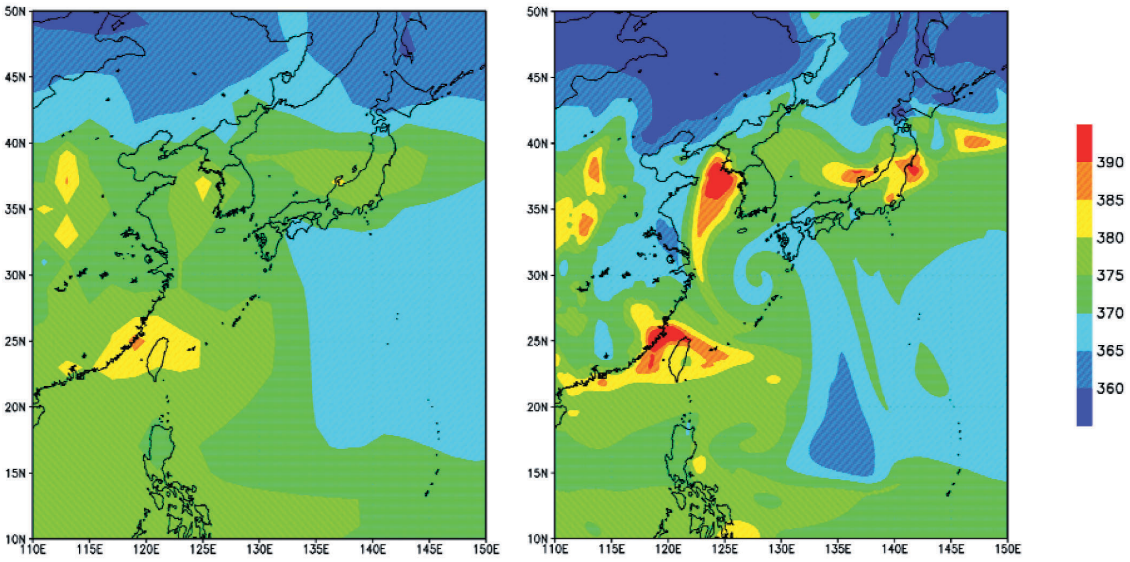

Fig. 5 Surface CO_2 concentrations at 03Z30AUG 2002 obtained from (a) 2×2 degrees (left) and (b) 0.25×0.25 degree (right) horizontal resolution simulation.

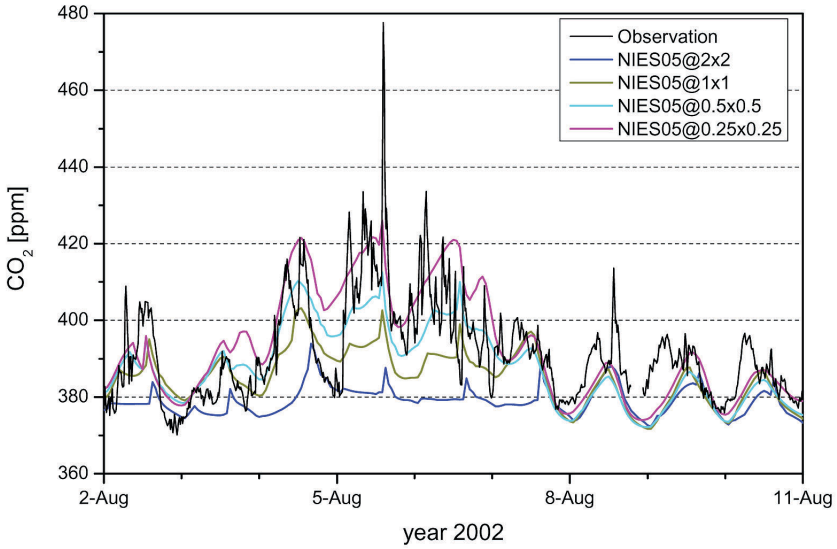

Fig. 6 Results of NIES05 at four kinds of resolutions at Tsukuba (36.05˚N, 140.13˚E) 200m high tower, which is in close proximity of megacity Tokyo (35.66˚N, 139.75˚E), and is occasionally under the influence of strong anthropogenic sources (an episode of up to about 70 ppm on 5th afternoon). An offset of 373 ppm is added to the model values for comparison with observations. The model sampling grids are located at (37˚N, 141˚E), (36.5˚N, 140.5˚E), (36.25˚N, 140.25˚E) and (36.13˚N, 140.13˚E) in 2×2˚, 1×1˚, 0.5×0.5˚ and 0.25×0.25˚ model resolutions, respectively.

are conducted using synthetic data experiments in time-independent inversion mode for 22, 42 or 432 region divisions of the globe (Maksyutov et al., 2003a; 2003b; Patra et al., 2002; 2003a; 2003b). Multi-model intercomparisons of time-independent and time-dependent CO_2 flux inversions are done under the TransCom3 project (Gurney et al., 2002, 2003, 2004; Law et al., 2003, Baker et al., 2006; Patra et al., 2006a). The inverted fluxes corresponding to NIES/FRCGC model are found to be similar to most other 12 or 16 participating models.

Figure 7 shows the TDIM estimated fluxes for the period 1979–2005 using NIES/FRCGC forward model simulations driven by interannually varying winds (TDI/64-IAV), and cyclostationary winds and CO_2 measurements at 67 stations (TDI/64-CYC/67) and 19 stations (TDI/64-CYC/19). Use of cyclostationary winds and smaller CO_2 data network significantly reduces the interannual variability in TDIM derived CO_2 fluxes for both the land and ocean regions (see Patra et al., 2006b for a discussion). However, the trends in fluxes are fairly independent of the forward model transport. Total land and ocean sinks appear to be increasing over the 1980–2005 periods (Fig. 7a, b) though the interannual variability has large influence on the trends derived, i.e., selection of period for trends estimation has measureable impact on the value itself. Similar is the situation for regional flux trends. Recently, trends in CO_2 exchange over the Southern Ocean (SO) have drawn considerable attention (see LeQuere et al., 2007 and references therein). Their analysis also use results from an atmospheric-CO_2 inversion that employs independent technique and derives fluxes at forward model grid resolution (Rodenbeck, 2005). Our model results also suggest a decrease in SO CO_2 sink in the past 2.5 decades but the magnitude of net decrease can be debated and vary between 0.04-0.1 Pg-C/decade depending on period of the fits, and appears to follow the trends in AAO (Fig. 7c). More detailed look in to the fluxes corresponding to northern (40–60˚S) and southern (60–80˚S) parts of SO suggests that the former region tending to become a weaker sink of CO_2 (Fig. 7d), where the biological uptake is prominent. In contrast, the net release from southern part indicates a decrease over our analysis period where the sea-air CO_2 exchange is believed to be controlled by coastal upwelling.

Greater flux anomalies estimated using 64-region inverse model and observations at 87-stations have generated curiosity in the scientific community (e.g., McKinley et al., 2006). The flux variability for total land and ocean show good correspondence with ENSO cycle and vary in opposite phase with each other (Fig. 7a, b). The amplitude and phase correspondence weakens for total ocean flux variability if atmospheric-CO_2 data at smaller num-

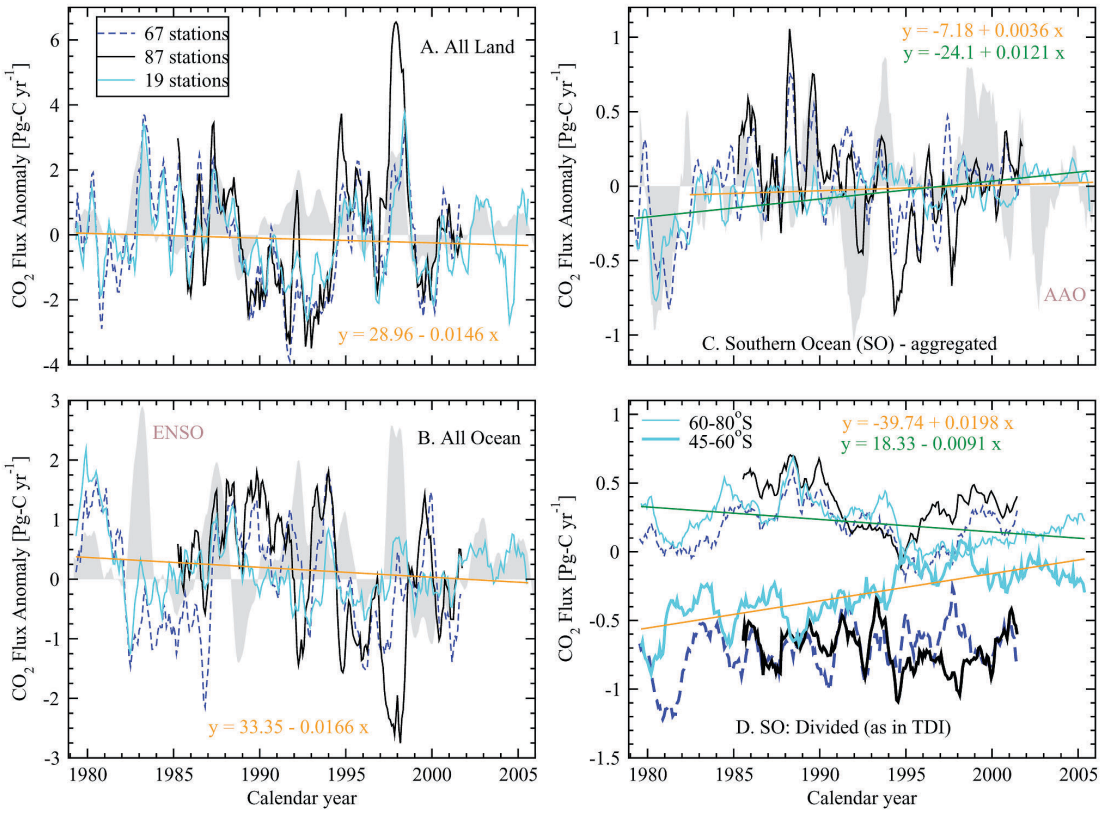

Fig. 7 Long-term trends and inter-annual variability in global and regional in CO_2 fluxes as derived by 64-region TDI model are depicted for the period 1979-2005. The NIES/FRCGC model is used for forward transport simulations and atmospheric CO_2 data are taken from three different observation networks consisting of 87, 67 and 19 stations. Linear fits to the fluxes using 19 stations network are shown as straight lines (panels A and B: orange line, Panel C: green and orange lines for 1979–2005 and 1982–2005 periods, respectively, Panel D: green and orange lines for southern and northern SO parts, respectively). In Panel D, absolute fluxes for two SO regions as in the TDIM are shown: thick and thin lines are for northern and southern parts, respectively. Note all other panels show flux anomalies. The shaded curves are for El Niño Southern Oscillation (ENSO; source: www.cdc.noaa.gov) and Antarctic Oscillation (AAO; source: www.cpc.ncep.noaa.gov) indices.

ber of sites is used in TDIM calculation, and amplitude of total land flux variability reduces although the phase remains fairly similar. Comparison of TDI/64-IAV derived flux anomalies with the estimates based on observations have been done for some of the ocean regions (Patra et al., 2005a). Both approaches result in similar magnitudes in flux anomalies for Equatorial Pacific, North Atlantic and North Pacific. Using an ocean biogeochemical elemental cycling model, sensitivity studies indicate flux anomalies to changes in nutrient supply through dust deposition from the atmosphere can partly explain the TDI/64-IAV derived CO_2 flux anomalies (see Patra et al., 2007 for details). The full range of IAVs for the ocean regions are encompassed by the sensitivity runs selected in that analysis when the dust-iron input is varied by ten times or one-tenth.

For the land regions, analysis using a simulation setup of Biome-BGC terrestrial ecosystem model underestimated the TDI estimated flux variability (Patra et al., 2005b), and they attributed the mismatch between the two to the lack biomass burning processes in Biome-BGC model. Reliable estimates of monthly-mean CO_2 fluxes due to fires (referred to as fire CO_2 flux) for several years have now been produced based on satellite derived burned area estimates, CASA terrestrial ecosystem model based fuel load inventories and known emission factors (van der Werf et al., 2006; version GFED2). Figure 8 shows a comparison of Biome-BGC net ecosystem exchange (NEE) and fire CO_2 flux (bottom-up estimate) with that estimated by TDI/64-IAV (top-down). For most of the years, the bottom-up and top-down estimates agree very well (difference within 10%), with the exception of Boreal Asia region for the period 1999–2000 only. This comparison further enhances our confidence in the derived flux IAV in the TDI/64-IAV inversion.

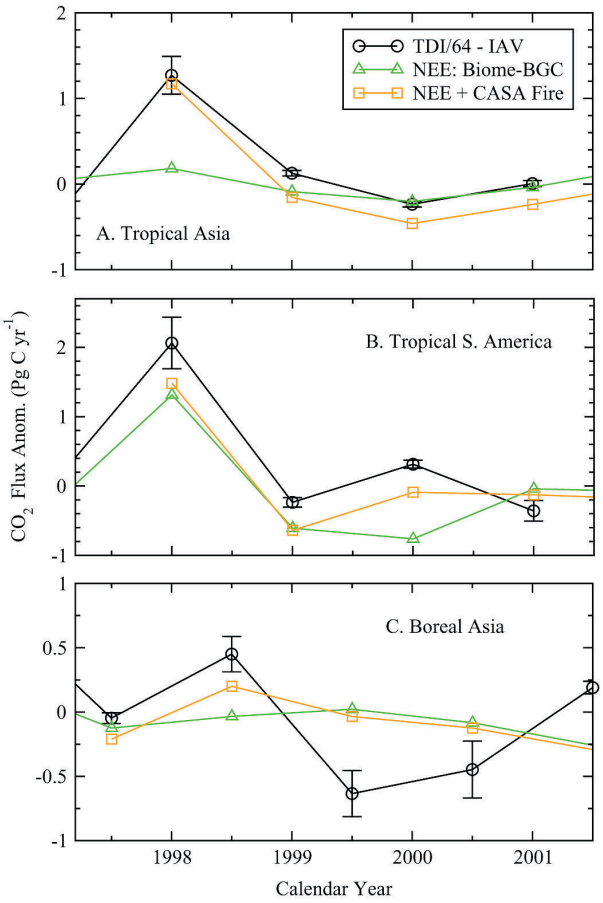

Fig. 8 The inverse modeling results for selected land regions. Biome-BGC + GFED2 fire match with TDI fluxes (observation network of 87 stations case).

6. Conclusions

Our "off-line" global atmospheric tracer transport model features a blend of established and newer approaches to representing the physical processes in the atmosphere important for atmospheric tracer transport. The semi-Lagrangian transport algorithm is combined with climatological PBL scheme and penetrative cloud convection parameterization to give a model capable of simulating the variations of the atmospheric tracers at a monthly and longer time scales. The chosen combination of the parameterizations proved to be effective in reproducing observed vertical and horizontal distributions of the passive atmospheric constituents with accuracy similar to those of the established atmospheric transport models. Test problems suite included transport of radon-222 as in WCRP transport model intercomparison experiment, sulfur hexafluoride (SF_6) following TransCom 2 model intercomparison, and CO_2 as in TransCom 1 intercomparison experiments. Vertical profiles of radon-222 are simulated successfully except for some possible underestimation of the surface concentrations in summer. The simulations of the long-lived tracers SF_6 and CO_2 demonstrated satisfactory performance in the interhemispheric transport. Strength of interhemispheric gradient in tracer transport is important for realistic estimation of sources/sinks estimation using inverse modeling of atmospheric CO_2 and satisfactory results are obtained for annual and monthly mean flux inversions. We have reviewed the CO_2 sources/sinks inversion results using a 64-region time-dependent inverse model using atmospheric CO_2 data and NIES/FRCGC transport model driven by interannually varying meteorology. Some recent developments in capturing the interannual variations in CO_2 fluxes and short-term trends are discussed. Our model results are supported by other independent estimates. Further tests and improvements in the forward transport model design are achieved for better simulation of day-to-day and diurnal variability in the tracer concentrations. The newer model version (NIES05) uses diurnally varying PBL (3-hour interval), and 6-hourly pressure level meteorological parameters (U, V, T etc.). This model is run at one of the finest horizontal resolution (0.25˚×0.25˚) globally and 47 layers. The finest resolution simulation shows remarkable improvements for matching the observations from a tower near to the megacity Tokyo.

Acknowledgment

We are grateful to H. Akimoto and G. Inoue for supporting this research at FRCGC and NIES. The global meteorological analysis data were provided by the ECMWF, NASA/GSFC DAO, and NCEP/NCAR. Authors thank M. Heimann for providing information on TM2 model design that facilitated development of our cumulus parameterization scheme. This work is benefited from discussions with S. Taguchi and Y. Takayabu. Thanks are due to the reviewers for useful comments to improve the manuscript.

References

[1] H. Akimoto, S. Maksyutov, and H. Ueda, Three-dimensional numerical model of atmospheric pollutant transport and transformation. - In: *Proc. 2-nd Symposium of Supercomputer Society*, Tokyo, Nov. 1992, CRC Research Institute, pp.18–23, 1993.

[2] D. F. Baker, et al., TransCom 3 inversion intercomparison: Impact of transport model errors on the interannual variability of regional CO_2 fluxes, 1988–2003, *Global Biogeochem. Cycles*, vol.**20**, GB1002, 2006.

[3] B. Bolin and C.D. Keeling, Large scale atmospheric mixing as deduced from seasonal and meridional variations of the atmospheric carbon dioxide, *J. Geophys. Res.*, vol.**68**, pp.3899–3920, 1963.

[4] CIESIN, The Center for International Earth Science Information Network, Earth Institute, Columbia University,

New York (www.ciesin.columbia.edu), 2000.

[5] P. Courtier, E. Andersson, W. Heckley, J. Paillex, et al., The ECMWF implementation of the three-dimensional variational assimilation (3D-Var), I, Formulation, *Quart. J. Roy. Meteor. Soc*., vol.**124**, pp.1783–1807, 1998.

[6] A. S. Denning, D. A. Randall, Collatz, and P. J. Sellers, Simulations of terrestrial carbon metabolism and atmsopheric CO_2 in a general circulation model, Part 2: Simulated CO_2 concentrations, *Tellus*, vol.**48B**, pp.8543–8567, 1996.

[7] A. S. Denning, M. Holzer, K. R. Gurney, M. Heimann, et al., Three-dimensional transport and concentration of SF_6: A model intercomparison study (TransCom 2), *Tellus*, vol.**51B**, pp.266–297, 1999.

[8] F. Dentener, J. Feichter and A. Jeuken, Simulation of the transport of Rn222 using on-line and off-line global models at different horizontal resolutions: a detailed comparison with measurements, *Tellus*, vol.**51B**, pp.573–602, 1999.

[9] ECMWF, ECMWF/WCRP Level III-A Global Atmospheric Data Archive, ECMWF (http://www.ecmwf.int), 1999.

[10] L. S. Geller, J. W. Elkins, J. M. Lobert, A. D. Clarke, D. F. Hirst, J. H. Butler and R. C. Meyers, Tropospheric SF_6: Observed latitudinal distribution and trends, derived emissions and interhemispheric exchange time. *Geophys. Res. Lett*., vol.**24**, pp.675–678, 1997.

[11] G. Grell, J. Dudhia, and D. Stauffer, A Description of the Fifth-Generation Penn State/NCAR Mesoscale Model (MM5), *NCAR/TN-398*, pp.122, 1995.

[12] S. Gold, H. Barkhau, W. Shleien, and B. Kahn, Measurement of naturally occurring radionuclides in air. In: *The natural radiation environment*, edited by J.A.S. Adams and W.M.Lowder, Univ. of Chicago Press, Chicago, Ill., pp.369–382, 1964.

[13] K. R. Gurney, R. M. Law, P. J. Rayner, and A. S. Denning, TransCom-3 experimental protocol, *Paper No. 707*, Dept. Atmos. Sci., Colo. State Univ., 2000.

[14] K. R. Gurney and Transcom3 modellers, Towards robust regional estimates of CO_2 sources and sinks using atmospheric transport models, *Nature*, vol.**415**, pp.626–630, 2002.

[15] K. R. Gurney and Transcom3 modellers, TransCom-3 CO_2 inversion intercomparison: 1. Annual mean control results and sensitivity to transport and prior flux information, *Tellus*, vol.**55B**, pp.555–579, 2003.

[16] K. R. Gurney and Transcom3 modellers, Transcom 3 inversion intercomparison: Model mean results for the estimation of seasonal carbon sources and sinks, *Global Biogeochem. Cycles*, vol.**18**, GB1010, 2004.

[17] J. J Hack, B. A. Boville, B. P. Briegleb, J. T. Kiehl, P. J. Rasch, and D. L. Williamson, *Description of the NCAR community climate model (CCM2)*, NCAR/TN-382, pp.108, 1993.

[18] M. Heimann and C. D. Keeling, A three dimensional model of atmospheric CO_2 transport based on observed winds: 2. Model description and simulated tracer experiments. In: *Aspects of Climate Variability in the Pacific and the Western Americas*, Ed. D. H. Peterson, American Geophysical Union, Washington DC, pp.237–275, 1989.

[19] M. Heimann, The TM2 tracer model, model description and user manual, *DKRZ Report*, *No.10*, Hamburg, pp.47, 1995.

[20] R. Hein, P. J. Crutzen, and M. Heimann, An inverse modeling approach to investigate the global atmospheric methane cycle, *Global Biogeochem Cycles*, vol.**11**, pp.43–76, 1997.

[21] D. J. Jacob, M. J. Prather, S. C. Wofsy, and M. B. McElroy, Atmospheric distribution of ^{85}Kr simulated with a general circulation model, *J. Geophys. Res*., vol.**92**, pp.6614–6626, 1987.

[22] D. Jacob, M. J. Prather, P. J. Rasch, R.-L. Shea et al., Evaluation and intercomparison of global transport models using ^{222}Rn and other short-lived tracers., *J. Geophys. Res*. vol.**102**, no.D5, pp.5953–5970, 1997.

[23] M. A. Kritz, J.-C. Le Roulley, and E. F. Danielsen, The China Clipper, Fast advective transport of radon-rich air from the Asian boundary layer to the upper troposphere near California, *Tellus*, vol.**42B**, pp.46–61, 1990.

[24] G. Lambert, G. Polian, B. Ardouin, J. Renault, and Y. Balkanski, *CFR Database of ^{222}Rn, ^{220}Rn and ^{210}Pb in Subantarctic and Antarctic atmosphere*, Centre des Faibles Radioactiv., Gif-sur-Yvette, France, 1995.

[25] R. Law, P. Rayner, A.S. Denning, D. Erickson, et al., Variations in the modelled atmospheric transport of carbon dioxide and its consequences for CO_2 inversions, *Global Biogeochem. Cycles*, vol.**10**, pp.783–796, 1996.

[26] R. M. Law and Transcom3 modellers, TransCom 3 CO_2 inversion intercomparison: 2. Sensitivity of annual mean results to data choices, *Tellus*, vol.**55B**, pp.580–595, 2003.

[27] R. M. Law, W. Peters, and C. Rödenbeck, Protocol for TransCom continuous data experiment, *Purdue Clim. Change Res. Center Tech. Rep*., (www.purdue.edu; path:/transcom/pdf/transcom/protocol_v5.pdf), 2006.

[28] C. Le Quéré, C. Rödenbeck, E. T. Buitenhuis, T. J. Conway, R. Langenfelds, A. Gomez, C. Labuschagne, M. Ramonet, T. Nakazawa, N. Metz, N. Gillett, and M. Heimann, Weakening of the Southern Ocean sink of CO_2, *Science*, vol.**316**, 2007.

[29] I. Levin and V. Hesshaimer, Refining of atmospheric transport model entries by the globally observed passive tracer distributions of ^{85}Kr and sulfur hexafluoride (SF_6), *J. Geophys. Res*., vol.**101**, pp.16745–16755, 1996.

[30] M. Maiss, L. P. Steele, R. J. Francey, P. J. Fraser, R. L. Langefelds, N. B. A. Trivett, and I. Levin, Sulfur hexafluoride – a powerful new atmospheric tracer, *Atmos. Environ.*, vol.**30**, pp.1621–1629, 1996.

[31] N. M. Mahowald, R. G. Prinn, and P. J. Rasch, Deducing CCl_3F emissions using an inverse method and a chemical

transport model with assimilated winds, *J. Geophys. Res.*, vol.**102**, pp.28127–28138, 1997.

[32] S. Maksyutov, Short-term simulations of atmospheric methane concentrations with a global tracer transport model. In: *International Symposium on Global Cycles of Atmospheric Greenhouse Gases*, Sendai, Japan, pp.333–336, 1994.

[33] S. Maksyutov and G. Inoue, Vertical profiles of radon and CO_2 simulated by the global atmospheric transport model. In: *CGER Supercomputer activity report*, *CGER-I039–2000*, CGER NIES, Tsukuba, Japan, vol.**7**, pp.39–41, 2000.

[34] S. Maksyutov, D. Fujita, T. Saeki, and T. Nakazawa, Tracer transport model validation and model-simulated CO_2 cycle over continents, *EOS Trans*., vol.**81**, no.48, *AGU Fall Meet. Suppl*., abstract B21F-08, 2000.

[35] S. Maksyutov, P. K. Patra, and G. Inoue, Pseudo-data inversion of column-CO_2 observations by remote sensing using a high resolution inverse model, *Int. Archives of Photogrammetry*, *Remote Sensing and Spatial Inform. Sci*., *Vol.XXIV*, Part. 7/W14, 2003a.

[36] S. Maksyutov, T. Machida, H. Mukai, P. K. Patra, T. Nakazawa, G. Inoue, and TransCom-3 modelers, Effect of recent observations on Asian CO_2 flux estimates with transport model inversions, *Tellus*, vol.**55**, no.2, pp.522–529, 2003b.

[37] G. Marland, Fossil fuels CO_2 emissions: Three countries account for 50% in 1986 - In: *CDIAC Communications*, Winter 1989, pp.1–4, 1989.

[38] G. A. McKinley, et al., North Pacific carbon cycle response to climate variability on seasonal to decadal timescales, *J. Geophys. Res*., vol.**111**, C07S06, 2006.

[39] P. K. Patra and S. Maksyutov, Incremental approach to the optimal network design for CO_2 surface source inversion, *Geophys. Res. Lett*., vol.**29**, no.10, 1459, 2002.

[40] P. K. Patra, S. Maksyutov, and TransCom-3 modelers, Sensitivity of Optimal Extension of CO_2 Observation Networks to Model Transport, *Tellus*, vol.**55**, no.2, pp.498–511, 2003a.

[41] P. K. Patra, S. Maksyutov, Y. Sasano, H. Nakajima, G. Inoue, and T. Nakazawa, An evaluation of CO_2 observations with Solar Occultation FTS for Inclined-Orbit Satellite sensor for surface source inversion, *J. Geophys. Res*., vol.**108**, no.D24, 4759, 2003b.

[42] P. K. Patra, M. Ishizawa, S. Maksyutov, T. Nakazawa, and G. Inoue, Role of biomass burning and climate anomalies for land-atmosphere carbon fluxes based on inverse modeling of atmospheric CO_2, *Global Biogeochem. Cycles*, vol.**19**, GB3005, 2005a.

[43] P. K. Patra, S. Maksyutov, M. Ishizawa, T. Nakazawa, T. Takahashi, and J. Ukita, Interannual and decadal changes in the sea-air CO_2 flux from atmospheric CO_2 inverse modelling, *Global Biogeochem. Cycles*, vol.**19**, GB4013, 2005b.

[44] P. K. Patra, S. Maksyutov, and T. Nakazawa, Analysis of atmospheric CO_2 growth rates at Mauna Loa using inverse model derived CO_2 fluxes, *Tellus*, vol.**57B**, pp.357–365, 2005c.

[45] P. K. Patra and Transcom3 modellers, Sensitivity of inverse estimation of annual mean CO_2 sources and sinks to ocean-only sites versus all-sites observational networks, *Geophys. Res. Lett.*, vol.**33**, L05814, 2006a.

[46] P. K. Patra, S. E. Mikaloff-Fletcher, K. Ishijima, S. Maksyutov, and T. Nakazawa, Comparison of CO_2 fluxes estimated using atmospheric and oceanic inversions, and role of fluxes and their interannual variability in simulating atmospheric CO_2 concentrations, *Atmos. Chem. Phys. Discuss*., vol.**6**, pp.6801–6823, 2006b.

[47] P. K. Patra, J. K. Moore, N. Mahowald, M. Uematsu, S. C. Doney, and T. Nakazawa, Exploring the sensitivity of basin-scale air-sea CO_2 fluxes to interannual to decadal variability in atmospheric dust deposition using ocean carbon models and atmospheric CO_2 inversions, *J. Geophys. Res*., vol.**112**, G02012, 2007.

[48] N.A. Philips, A coordinate system having some special advantages for numerical forecasting, *J. Meteorol*., vol.**14**, pp.184–185, 1957.

[49] P. Pochanart, H. Akimoto, S. Maksyutov, and J. Staehelin, Surface ozone at the Swiss alpine site Arosa: the hemispheric background and the influence of the large scale atmospheric emissions, *Atmos. Environ.*, vol.**35**, pp.5553–5566, 2001.

[50] M. Prather, M. McElroy, S. Wofsy, G. Russel, and D. Rind, Chemistry of the global troposphere: Fluorocarbons as tracers of air motion, *J. Geophys. Res*., vol.**92**, pp.6579–6613, 1987.

[51] P. J. Rasch, B. A. Boville, and G. P. Brasseur, A three-dimensional general circulation model with coupled chemistry for the middle atmosphere, *J. Geophys. Res*, vol.**100**, pp.9041–9071, 1995.

[52] A. R. Ravishankara, S. Solomon, A. A. Turnispeed, and R. F. Warren, Atmospheric lifetimes of long-lived halogenated species, *Science*, vol.**259**, pp.194–199, 1993.

[53] P. J. Rayner, I. G. Enting, R. J. Francey, and R. Langenfelds, Reconstructing the recent carbon cycle from atmospheric CO_2, $\delta^{13}C$ and O_2/N_2 observations, *Tellus*, vol.**51B**, pp.213–232, 1999.

[54] C. Rödenbeck, Estimating CO_2 sources and sinks from atmospheric mixing ratio measurements using a global inversion of atmospheric transport, *Max-Planck-Institute for Biogeochemistry*, *Tech. Rep. 6*, P.O. Box 100164, 07701 Jena, Germany, 2005 (http://www.bgc-jena.mpg.de;path: /mpg/websiteBiogeochemie/Publikationen/Technical_Reports/tech_report6.pdf).

[55] S. Schubert, R. Rood, and J. Pfaendtner, An assimilated

dataset for Earth science applications, *Bull. Am. Meteorol. Soc*., vol.**74**, pp.2331–2342, 1993.

[56] S. Taguchi, A three-dimensional model of atmospheric CO_2 transport based on analyzed winds: model description and simulation results for TRANSCOM, *J. Geophys. Res*., vol.**101**, pp.15099–15109, 1996.

[57] T. Takahashi, S. C. Sutherland, C. Sweeney, A. Poisson, N. Metzl, B. Tilbrook, N. Bates, R. Wanninkhof, R. A. Feely, C. Sabine, J. Olafsson, and Y. Nojiri, Global sea-air CO_2 flux based on climatological surface ocean pCO_2, and seasonal biological and temperature effects, *Deep-Sea Research Part II*, vol.**49**, pp.1601–1622, 2002.

[58] P. Tans, I. Fung, and T. Takahashi, Observational constraints of the global atmospheric CO_2 budget, *Science*, vol.**247**, pp.1431–1438, 1990.

[59] M. Tiedtke, A comprehensive mass flux scheme for cumulus parameterization in large-scale models, *Mon. Wea. Rev*., vol.**117**, pp.1779–1800, 1989.

[60] Y. Tohjima, H. Mukai, S. Maksyutov, Y. Takahashi, T. Machida, M. Utiyama, M. Katsumoto, and Y. Fujinuma, Variations in atmospheric nitrous oxide observed at Hateruma monitoring station, *Chemosphere-Global Change Science*, vol.**2**, pp.435–443, 2000.

[61] Y. Tohjima, T. Machida, M. Utiyama, M. Katsumoto, Y. Fujinuma, S. Maksyutov, Analysis and presentation of in situ atmospheric methane measurements from Cape Ochiishi and Hateruma Island, *J. Geophys. Res*., vol.**107**, no.D12, 4148, 2002.

[62] G. R. van der Werf, J. T. Randerson, L. Giglio, G. J. Collatz, P. S. Kasibhatla, and A. F. Arellano Jr, Interannual variability in global biomass burning emissions from 1997 to 2004, *Atmos. Chem. Phys*., vol.**6**, pp.3423–3441, 2006.

[63] WDCGG, WMO World Data Centre for Greenhouse Gases, Japan Meteorological Agency, Tokyo (http://gaw.kishou.go.jp), 2007.

[64] W. M. Washington and C. L. Parkinson, *An introduction to three-dimensional climate modeling*, Oxford University Press, New York, pp.422, 1986.

[65] D.L. Williamson and P. J. Rasch, Two-Dimensional Semi-Lagrangian Transport with Shape Preserving Interpolation, *Mon. Wea. Rev*., vol.**117**, pp.102–129, 1989.

[66] D.L. Williamson and R. Laprise, Numerical approximations for global atmospheric GCMs – In: *Numerical modeling of global atmosphere in the climate system*. Ed. P. Mote and A. O'Neil, NATO Science Series, Kluwer Academic Publishers, Series C, vol.**550**, pp.127–220, 2000.

[67] P. H. Zimmermann, J. Feichter, H. K. Rath, P. J. Crutzen, and W. Weiss, A global three-dimensional source-receptor model investigation using ^{85}Kr, *Atmos. Environ*., vol.**23**, pp.25–35, 1989.